Available online at www.sciencedirect.com
ScienceDirect
Trans. Nonferrous Met. Soc. China 35(2025) 1212−1232
Transactions of Nonferrous Metals Society of China
www.tnmsc.cn

Influence of process parameters on microstructure and properties of Cu−Cr−Nb−Y alloy manufactured by laser powder bed fusion

Shu-peng YE, Zu-ming LIU, Ya-zhou ZHANG, Tao LIU, Dao-yan JIANG, Lei CHEN, Cai CHEN

State Key Laboratory of Powder Metallurgy, Central South University, Changsha 410083, China

Received 12 October 2023; accepted 11 May 2024

Abstract: A novel Cu−4.8Cr−2.2Nb−0.15Y (at.%) alloy was fabricated by employing the laser powder bed fusion with different processing parameters. The influence of laser power (P), scanning speed (v), and laser linear energy density (E_l) on the defects, melt pool morphology, microstructure, and properties of the alloy was systematically investigated. The results show that the optimized process parameters for preparing Cu−Cr−Nb−Y alloy with relative density over 99.5% are P=300−350 W and v=650−800 mm/s, corresponding to E_l=0.375−0.538 J/mm. When E_l< 0.3 J/mm, increasing P or decreasing v can enhance the continuity and size of the melt pool, reduce the lack-of-fusion defects, and increase the relative density. However, excessively high E_l leads to a deeper melt pool, more keyholes, and reduced relative density. The grain size of the as-built Cu−Cr−Nb−Y alloy shows a bimodal distribution, with fine grains at the center and coarse grains at the edge of the melt pool. Increasing P or decreasing v increases the average grain size and ⟨110⟩ texture intensity. The alloy fabricated with P=350 W and v=800 mm/s displays the highest relative density of 99.82%. The yield strength, tensile strength, and elongation are (443±5) MPa, (699±4) MPa, and (17.1±0.7)%, respectively.

Key words: Cu−Cr−Nb−Y alloy; laser powder bed fusion; melt pool morphology; microstructure; mechanical properties

1 Introduction

Copper-based alloys have essential applications in various fields such as aerospace, nuclear energy, rail transportation, integrated circuits, and others, owing to their excellent electrical and thermal conductivity, as well as their mechanical properties [1−3]. Cu−Cr−Nb alloys have been developed by NASA specifically for high-heat-flux environments, such as rocket engine combustion chambers, due to their combination of high strength, high thermal conductivity, and good heat resistance [4,5]. However, casting processes often lead to the formation of large-sized Cr_2Nb phase with high melting point and high hardness [6−8]. The large-sized Cr_2Nb phase is difficult to regulate with subsequent processing, and results in reductions in the desirable properties of Cu−Cr−Nb alloys, thus posing notable challenges to the fabrication of Cu−Cr−Nb alloys through casting–deformation processing. On the other hand, the press molding process of chill-block melt spinning can produce Cu−Cr−Nb alloys with fine and uniformly distributed Cr_2Nb reinforcement phase [9]. Cu−Cr−Nb alloys with high relative density can be fabricated using hot extrusion of powders and vacuum hot pressing, resulting in Cr_2Nb phases with sizes less than 1 μm, and the tensile strength of fabricated Cu−8Cr−4Nb and Cu−4Cr−2Nb alloys reaches 500 MPa [10−13]. However, these fabrication methods for Cu−Cr−Nb alloys have the

Corresponding author: Zu-ming LIU, Tel: +86-13975809336, E-mail: lzm@csu.edu.cn
DOI: https://doi.org/10.1016/S1003-6326(24)66744-0

disadvantages of long preparation cycles and high costs in the fabrication of complex geometric parts. Laser powder bed fusion (LPBF) is an advanced manufacturing technique that uses high-energy lasers to selectively melt metal powders layer by layer. This process has attracted considerable research interest and has been employed to produce copper alloys with exceptional mechanical properties [14−16]. The high cooling rates (10^5−10^7 K/s) during the LPBF process enhance the supersaturated solid solubility of solute elements and result in fine-sized Cr_2Nb phases [17,18]. Subsequent heat treatment can improve the comprehensive performance of Cu−Cr−Nb alloys significantly [19]. Therefore, Cu−Cr−Nb alloys fabricated using LPBF can possess both good mechanical properties and thermal conductivity.

Copper and its alloys possess high laser reflectivity and thermal conductivity, which can typically lead to higher porosity and lower relative density when prepared using LPBF with infrared lasers (λ≈1070 nm) [20]. In contrast to pure copper, the significant volume fraction of the Cr_2Nb phase in Cu−Cr−Nb alloy powder can effectively reduce the laser reflectivity. Consequently, this promotes heat absorption and melting during the LPBF process [21,22]. Additionally, the presence of the Cr and Nb elements reduces the thermal conductivity of copper alloys. This characteristic aids in optimizing the LPBF process by reducing heat dissipation, thus improving the density of Cu−Cr−Nb alloys. Rare-earth elements play a beneficial role in enhancing the mechanical properties and conductivity of copper alloys. The addition of trace Ce into copper alloys enables a simultaneous improvement in conductivity and mechanical properties [23,24]. Additionally, rare-earth Y promotes the grain refinement in Cu−Cr−Zr alloys and accelerates the dynamic recrystallization behavior [25]. Therefore, adding rare-earth elements holds great promise for enhancing the properties of Cu−Cr−Nb alloys. The LPBF process parameters including laser power, scanning speed, hatch spacing, layer thickness, and substrate preheating temperature have a significant impact on the metallurgical defects and microstructure of the as-built alloy. Therefore, a systematic study on the influence of the LPBF process parameters on the melt pool morphology, defects, and microstructure is of great significance for the preparation of high-performance copper alloys. In recent years, extensive research has been conducted on the LPBF process parameters for various alloys, including stainless steel [26], Al alloys [27−29], Ni alloys [30−32], Ti alloys [33,34], Cu alloys [35,36], and others. These illustrate that process parameters have different effects on the defects and microstructure of different alloys.

In this study, a novel Cu−Cr−Nb−Y alloy is prepared using the LPBF process. The influence of the process parameters, including laser power, scanning speed, and laser linear energy density on defects, melt pool morphology, microstructure, and properties of the alloy is investigated. The microstructure and performance of the Cu−Cr−Nb−Y alloy are modulated using the LPBF process. The results of this study could be of great significance for developing high-performance Cu alloys.

2 Experimental

2.1 Powder batch

The powder batch used in this study was Cu−4.8Cr−2.2Nb−0.15Y alloy powder prepared using close-coupled nozzle argon gas atomization. The powder composition was analyzed using an inductively coupled plasma emission spectrometer (Thermo Fisher Scientific ICAP7000), as listed in Table 1. The actual density (ρ_{powder}) of the alloy powder was measured using the gas volume method according to ISO12154:2014 [37] and found to be 8.769 g/cm^3. The morphology and microstructure of the Cu−Cr−Nb−Y alloy powder were observed using a field emission scanning electron microscope (SEM, TESCAN MIRA3) and the particle size distribution of the alloy powder was analyzed using a laser particle size analyzer (Malvern Panalytical Mastersizer 3000). The results in Fig. 1 show that the powder size distribution ranged from 12 to 62 μm, with a concentrated particle size distribution and good sphericity. The presence of satellite and hollow powders was minimal, indicating good powder flowability of 0.432 s/g.

Table 1 Chemical composition of argon-atomized Cu−Cr−Nb−Y powder (at.%)

Cr	Nb	Y	Cu
4.8	2.2	0.15	Bal.

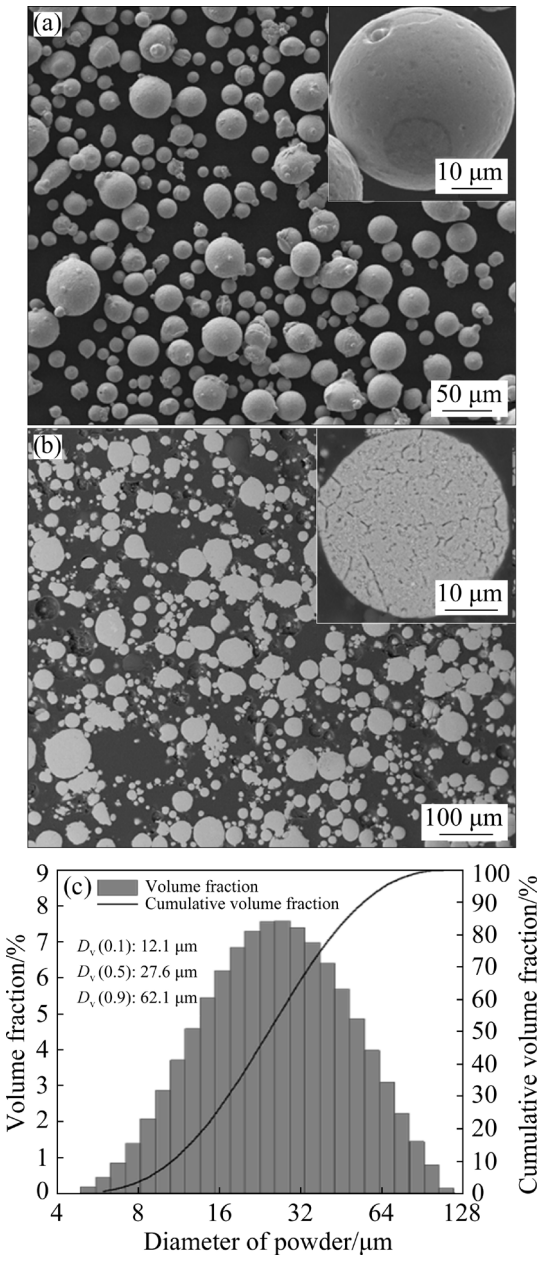

Fig. 1 Characteristics of argon-atomized Cu−Cr−Nb−Y powder: (a) Powder morphology; (b) Powder microstructure; (c) Powder size distribution

2.2 LPBF process

The LPBF process was conducted using an LPBF machine (Hunan Farsoon 271M), and the specific parameters are listed in Table 2. The scanning strategy is illustrated in Fig. 2(a). The dimensions of the as-built samples were 10 mm × 10 mm × 10 mm and 73 mm × 10 mm × 10 mm, and sample number, along with their corresponding process parameters, are presented in Table 3. The laser linear energy density (E_l) characterizing the comprehensive laser energy input in Table 2 was calculated using Eq. (1):

$$E_l=P/v \quad (1)$$

where P is the laser power and v is scanning speed.

Table 2 LPBF process parameters applied to Cu−4.8Cr−2.2Nb−0.15Y alloy

Parameter	Setting value
Laser power, P/W	150, 200, 250, 300, 350
Scanning speed, v/(mm·s^{-1})	500, 650, 800, 950, 1100
Hatch space, h/μm	80, 500
Layer thickness, t/μm	30
Alternating scanning strategy/(°)	67
Preheating temperature, T/°C	100
Linear energy density, E_l/(J·mm^{-1})	0.136−0.7

Figure 2 illustrates the LPBF scanning strategy and presents a schematic diagram of the tensile specimen. To investigate the influence of process parameters on the melt pool depth and simulate the powder melting and melt solidification that occurs during the LPBF, an additional layer of powder was spread on the top layer of the as-built sample. A single scanning was performed with a hatch space of 500 μm.

Table 3 Sample number and their corresponding LPBF parameters

Laser power/W	Scanning speed/(mm·s^{-1})				
	500	650	800	950	1100
150	*P*150*v*500	*P*150*v*650	*P*150*v*800	*P*150*v*950	*P*150*v*1100
200	*P*200*v*500	*P*200*v*650	*P*200*v*800	*P*200*v*950	*P*200*v*1100
250	*P*250*v*500	*P*250*v*650	*P*250*v*800	*P*250*v*950	*P*250*v*1100
300	*P*300*v*500	*P*300*v*650	*P*300*v*800	*P*300*v*950	*P*300*v*1100
350	*P*350*v*500	*P*350*v*650	*P*350*v*800	*P*350*v*950	*P*350*v*1100

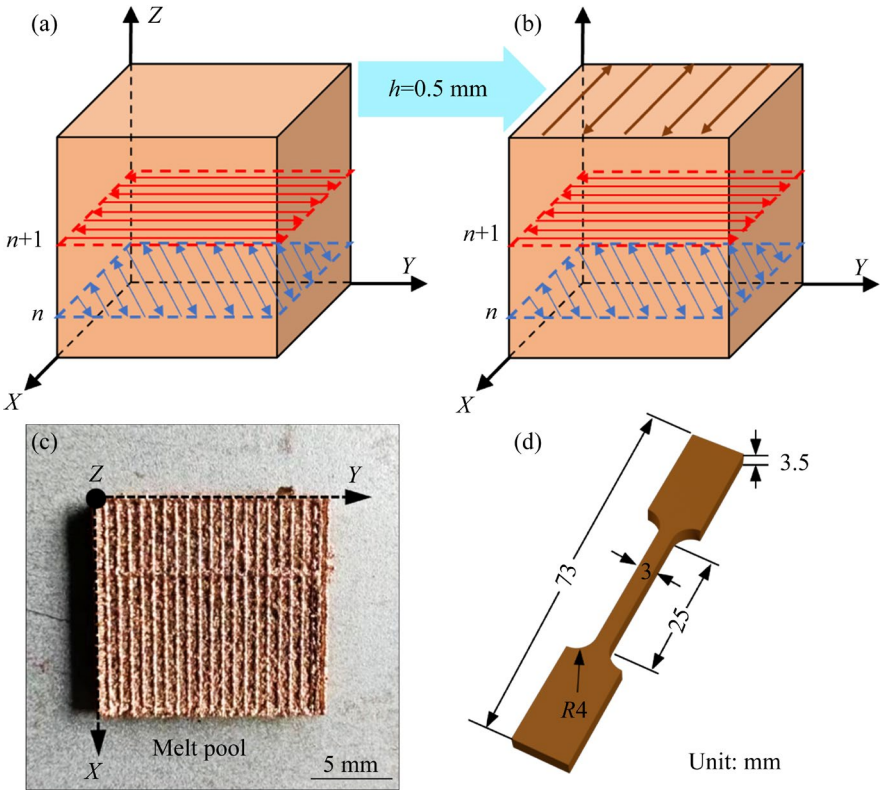

Fig. 2 Schematic diagrams of scanning strategy and tensile specimen: (a, b) Scanning strategy and single melt pool; (c) Top-view image of as-built sample; (d) Tensile specimen diagram

2.3 Analysis and characterization

The relative density was used to characterize the number of pores and other defects in the as-built alloy. The relative density was defined as the radio of the true density of as-built sample to the density of powder, where the true density of the as-built alloy was measured using the Archimedes drainage method (Sartorius MSA324S-000-DU).

The phase composition of the as-built Cu−Cr−Nb−Y alloy was analyzed using an X-ray diffractometer (XRD, Bruker Advance D8) with a scanning range of diffraction angle (2θ) from 20° to 90° and a scanning rate of 1 (°)/min. The pore defects of the as-built alloy were observed with an optical microscope (OM, Zhongxian MA2000). The SEM and electron backscatter diffraction (EBSD) images of the as-built microstructures were observed using a field emission scanning electron microscope (SEM, TESCAN MIRA3). The data acquisition step size for the EBSD analysis was 0.8 μm. The SEM and EBSD specimens were prepared using the as-built alloy, which were electrochemically etched using a voltage of 2 V for 10−20 s in solution of 40% H_2SO_4 + 10% H_3PO_4 + 50% DI water.

The microhardness of the as-built alloy was measured using a microhardness tester (Buehler MicroMet 5101), with a load of 200 g and a loading time of 15 s. The room-temperature tensile properties were tested using an electronic universal tensile testing machine (Instron 3369), with a strain rate of 1 mm/min. The dimensions of the tensile specimen are shown in Fig. 2(d), with the tensile direction perpendicular to the build orientation. The electrical conductivity of the as-built alloy was measured using a digital conductivity meter (Xinbote D60K). Each performance testing was repeated using three specimens, and the average value was taken as the experimental results.

3 Results and discussion

3.1 Pores and relative density

Metallographic microstructure images of the *XZ* plane (parallel to the build orientation) of the Cu−Cr−Nb−Y alloy are shown in Fig. 3. It can be observed that pores are the primary defects in the as-built alloy. When the laser power is low (P=150 W), irregular large-sized pores (indicated by yellow arrows) appear throughout the interior of

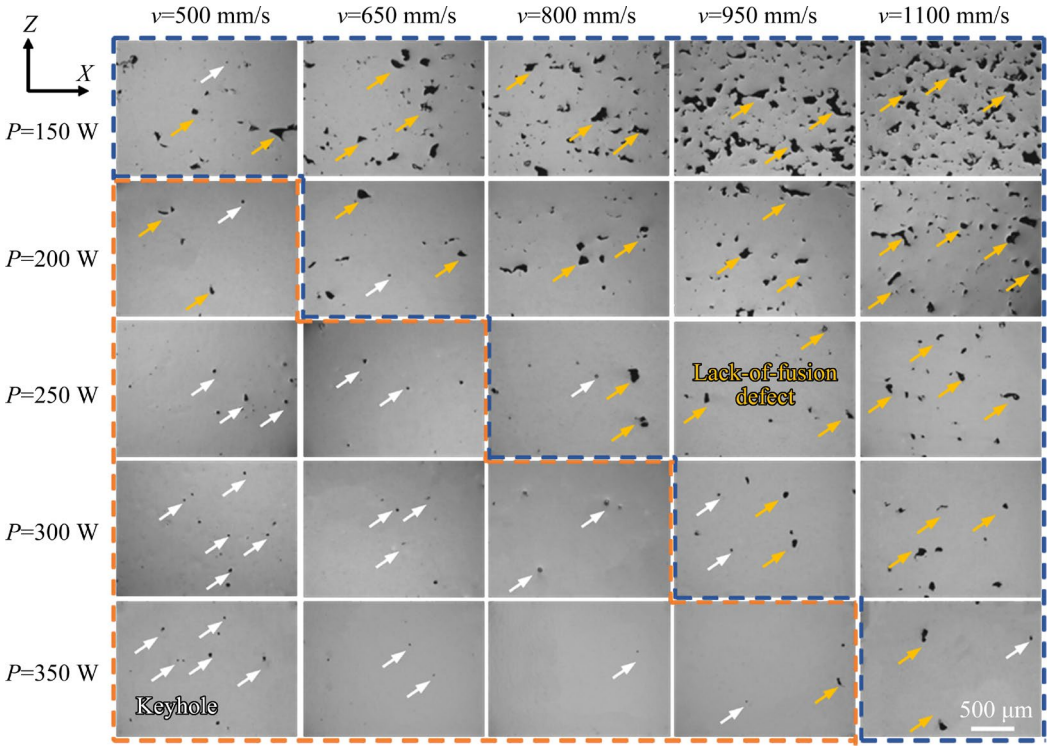

Fig. 3 Metallographic microstructure of Cu−Cr−Nb−Y alloy prepared with different process parameters (Yellow arrows indicate large irregular pores; White arrows indicate tiny circular pores)

the as-built alloy. As v increases from 500 to 1100 mm/s, both the number and size of the pores expand. Conversely, with an increase in P from 150 to 350 W, the size and number of irregular large-sized pores rapidly decrease. However, circular small-sized pores (indicated by white arrows) increase and become the main defects. When the laser power is high (P=350 W), as v increases from 500 to 800 mm/s, the number of small-sized pores gradually decreases, and no apparent defects are observed inside the samples prepared using v=800 mm/s. However, large-sized defects reappear when v>800 mm/s. Notably, when a lower scanning speed (v=500 mm/s) is used, the laser power significantly influences the type, number, and size of the pores. The results indicate that the minimum number and size of pore defects are achieved when P ranges from 300 to 350 W, and v ranges from 650 to 800 mm/s.

Figure 4 shows the pore defect morphology of the as-built alloy. The size and type of pores are closely related to the laser energy input. Figures 4(a−c), respectively, show large-sized pore defects in the following samples: $P150v800$ (E_l=0.19 J/mm), $P250v800$ (E_l=0.31 J/mm), and $P350v1100$ (E_l=0.32 J/mm). The edges of these large-sized pores are irregular in shape, containing unmelted powder inside, with sizes larger than 100 μm, and some pores measure 300 μm in size and larger. These pores are classified as lack-of-fusion (LOF) defects. The formation of such large-sized LOF defects is closely associated with insufficient energy input. In the LPBF process, a lower laser energy input leads to poor wettability between the solid phase and liquid phase, as well as poor bonding between built layers, resulting in melt balling and the generation of large-sized LOF defects [38−40]. Figure 4(d) shows small-sized pore defects in Sample $P350v800$ (E_l=0.44 J/mm). These pores are circular in shape, with sizes smaller than 50 μm, and are primarily located at the bottom of the melt pool; these pores are categorized as keyholes. Keyhole defects are caused by gas entrapment within the melt pool when the laser energy input is too high [41,42].

Figure 5 shows the relative density and porosity of the as-built alloy. Figure 5(a) indicates that the relative density of as-built alloy increases as P increases from 150 to 350 W. However, the effect of the scanning speed on the relative density varies with different laser powers. When P<200 W, the relative density decreases with increasing scanning

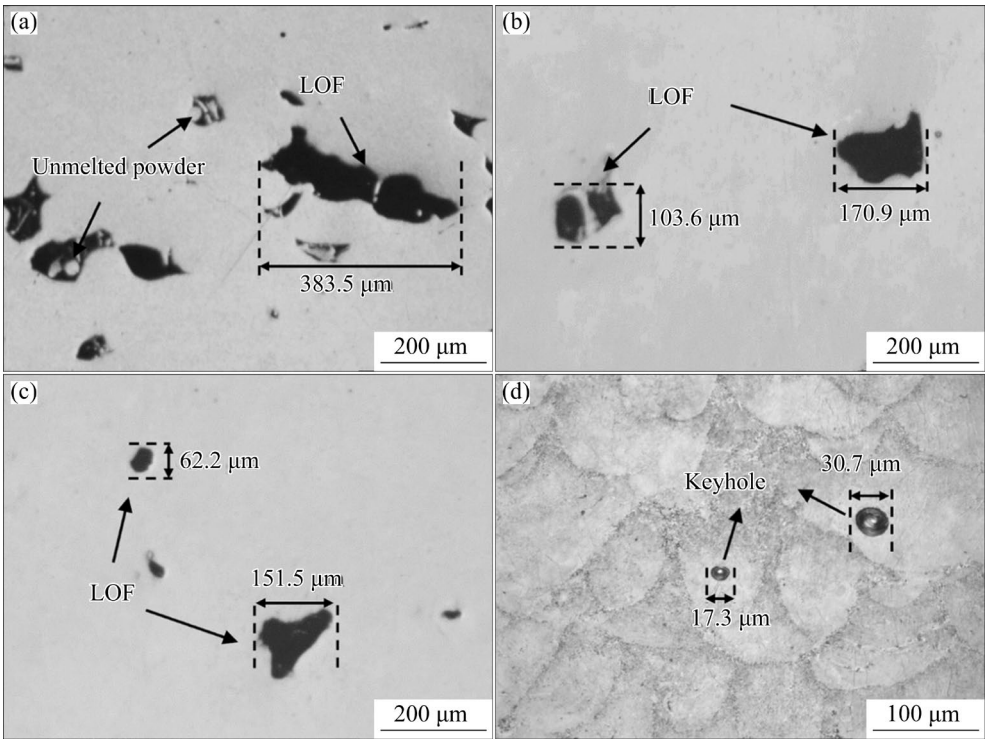

Fig. 4 Pore defect morphologies of Cu−Cr−Nb−Y alloy prepared with different process parameters: (a) LOF defects in Sample *P*150*v*800; (b) LOF defects in Sample *P*250*v*800; (c) LOF defects in Sample *P*350*v*1100; (d) Keyhole defects in Sample *P*350*v*800

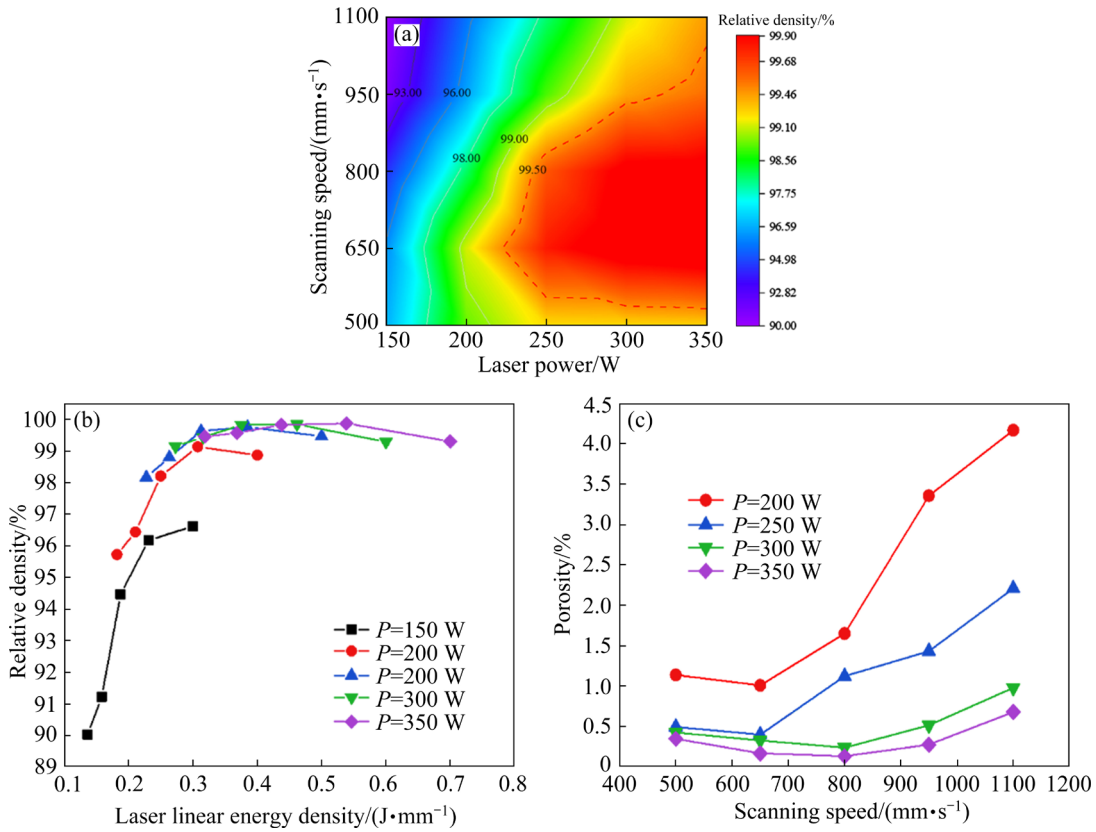

Fig. 5 Relative density and porosity of as-built Cu−Cr−Nb−Y alloy: (a) Influence of scanning speed and laser power on relative density; (b) Influence of laser linear energy density on relative density; (c) Influence of scanning speed and laser power on porosity

speed, and the relative density is less than 99%. Conversely, when P>200 W, the relative density initially increases and then decreases with increasing scanning speed. The relative density of the alloy can reach over 99.5% by using optimized process parameters of P=300−350 W and v=650−800 mm/s, and the highest relative density achieved is 99.82%, by using the parameters of P=350 W and v=800 mm/s.

Figure 5(b) shows the influence of the laser linear energy density on the relative density of the as-built alloy. It can be observed that, as the laser linear energy density increases, the relative density of the as-built alloy initially increases and then decreases. When E_l is less than 0.3 J/mm, a large number of LOF defects occur due to insufficient melting of Cu−Cr−Nb−Y alloy powder (Figs. 3 and 4), resulting in a relative density below 99% in the as-built alloy. When E_l is approximately 0.3 J/mm, the relative density of the as-built alloy prepared with different P and v values is significantly different, between 96.5% and 99.5%, because of the significant differences in the number and type of pore defects (Figs. 3 and 4). When E_l is greater than 0.3 J/mm, an increase in E_l leads to a reduction in the number and size of LOF defects (Fig. 3), resulting in the relative density of the as-built alloy exceeding 99%. When E_l is more than 0.5 J/mm, the excessive laser linear energy density leads to an increase in the number of keyhole defects (Figs. 3 and 4), and the relative density decreases. Comparatively, the impact of LOF defects on the relative density of the as-built alloy is more significant. The relative density of samples prepared with an E_l from 0.375 to 0.538 J/mm is greater than 99.5%, and the highest relative density for Sample P350v800 is prepared by using E_l=0.438 J/mm.

Figure 5(c) presents the influence of the scanning speed and laser power on the porosity. When the laser power increases, the porosity of as-built alloy decreases continuously. On the other hand, when the scanning speed increases, the porosity initially decreases and then increases. Notably, when P=350 W, the porosity of the as-built alloy fabricated with various scanning speeds is the lowest.

3.2 Melt pool morphology

The melt pool morphology plays a crucial role in determining the defects and relative density of the as-built alloy. Figure 6 shows the morphology of a single melt pool on the XY plane of the as-built alloy. It can be observed that when P≤200 W, the continuity of the melt pool is poor, with a large amount of unmelted powder (indicated by white arrows) and LOF defects (indicated by yellow arrows). As the laser power increases, the continuity of the melt pool improves. Conversely, when the laser power remains constant, an increase

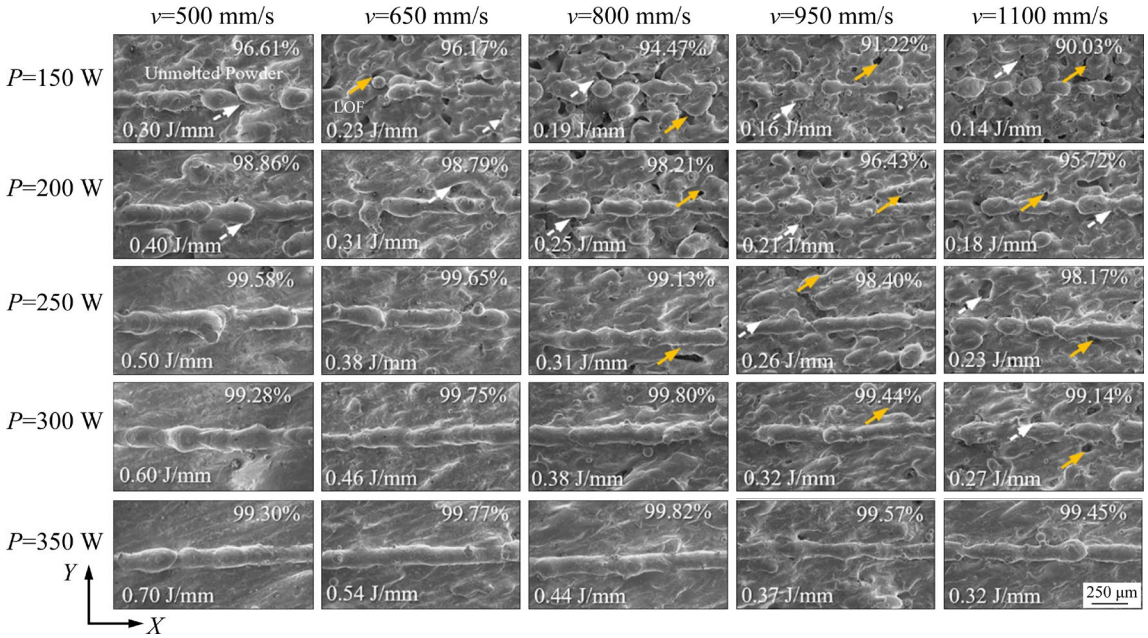

Fig. 6 SEM images of melt pool morphology prepared with different P and v values

in scanning speed leads to a decrease in the melt pool continuity. When P=350 W, the melt pools formed with various scanning speeds exhibit continuous features.

Figure 6 also presents the comprehensive effects of P and v, i.e., the laser linear energy density, on the continuity of the melt pool. The results show that when E_l≤0.3 J/mm, the melt pool is discontinuous, and the sample prepared with the minimum E_l, 0.14 J/mm, exhibits the poorest continuity of the melt pool and the lowest relative density. As E_l increases above 0.3 J/mm, the continuity of the melt pool improves, and the relative density of the samples increases. However, when E_l exceeds 0.5 J/mm, the melt pool remains continuous, but the relative density of the samples reduces.

By comparing the melt pool morphology of five samples with E_l=0.30−0.32 J/mm, namely, P150v500, P200v650, P250v800, P300v950, and P350v1100, it is found that there are significant differences in the continuity of melt pools prepared with similar E_l but different P and v values, which results in significant differences in relative density. As the laser power increases from 150 to 350 W, corresponding scanning speed increases from 500 to 1100 mm/s, the continuity of the melt pool improves, and the corresponding relative density of the as-built alloy obviously increases from 96.61% to 99.45%. This result indicates that the laser power and scanning speed have an essential influence on the continuity of the melt pool and relative density of the as-built alloy. When E_l of the LPBF is low, the metal powder cannot be fully melted, resulting in a higher dynamic viscosity and surface tension of the melt, causing melt balling and discontinuity of the melt pool [43]. This discontinuous melt pool leads to uneven powder spreading, further resulting in pore defects and a decrease in relative density.

Figure 7 demonstrates the influence of laser process parameters P and v on the melt pool morphology. Figure 7(a) shows that as the scanning speed increases, the melt pool depth initially decreases rapidly. The increase in laser power results in an elevated melt pool depth and the extent of rise is additionally influenced by the scanning speed. When the scanning speed is as high as 1100 mm/s, as the laser power increases from 150 to 350 W, the melt pool depth increases from 5 to 50 μm. However, the melt pool depth increases

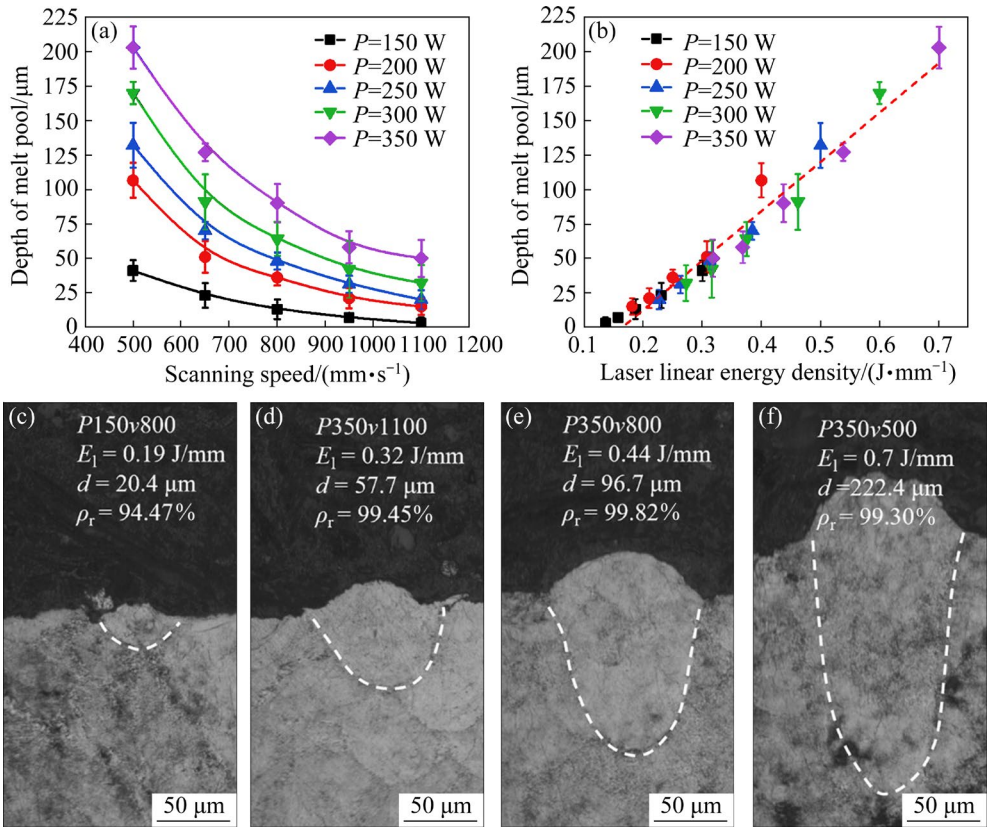

Fig. 7 Influence of process parameters on melt pool morphology: (a) Variation in depth of melt pool with P and v; (b) Variation in depth of melt pool with E_l; (c−f) Optical micrographs of several typical melt pool structures

approximately from 41 to 203 μm when the scanning speed is 500 mm/s. Overall, laser power has a more significant impact on melt pool depth, while scanning speed only exhibits a noticeable effect on the melt pool depth at high laser powers (P>200 W).

In order to comprehensively evaluate the influence of the laser parameters on the melt pool depth (d), the laser linear energy density E_l is used as an evaluation index of the laser parameters, according to Eq. (1), as shown in Fig. 7(b). It can be seen that the melt pool depth increases linearly with the increase in laser linear energy density E_l. The relationship between d and E_l is depicted by Eq. (2) [44], which shows a linear relationship between them:

$$d=E_l\cdot 2D/\sqrt{2\pi e}^{1/2}K\Delta T \quad (2)$$

where D is the thermal diffusivity, K is the thermal conductivity, and ΔT is the difference between the melting temperature and the preheating temperature.

Figures 7(c−f) show the optical micrographs of longitudinal cross-sections of melt pools prepared with different laser linear energy densities. It can be observed that the melt pool depth deepens as E_l increases. When E_l=0.19 J/mm (Sample P150v800), the depth of the melt pool is 20.4 μm (Fig. 7(c)), indicating a shallow melt pool in the conduction mode, with a large amount of LOF defects and unmelted powder (Fig. 4), and the sample exhibits a relative density of 94.47%. When E_l=0.32 J/mm (Sample P350v1100), the melt pool depth increases to 57.7 μm (Fig. 7(d)), and the melt pool changes to the transition mode, with a rapid decrease in the number of LOF defects and unmelted powder (Figs. 3 and 4), resulting in the relative density of the samples exceeding 99%. When E_l=0.44 J/mm (Sample P350v800), the melt pool depth increases to 96.7 μm (Fig. 7(e)), indicating a keyhole-mode melt pool, and the relative density of the as-built sample is the highest, reaching 99.82%. When the E_l further increases to 0.7 J/mm (Sample P350v500), the depth of the melt pool increases to 222.4 μm (Fig. 7(f)), leading to an increased number of keyholes (Figs. 3 and 4). Consequently, there is a slight decrease in the relative density of the as-built sample to 99.30%. Therefore, as the laser linear energy density increases, the melting mode of the melt pool changes from conduction mode to keyhole mode [35]. However, the higher laser linear energy density increases the depth of the melt pools (Figs. 7(e, f)), which leads to an increased number of keyholes (Figs. 3 and 4) and a decrease in the relative density (Fig. 5). The melt pool depth of samples prepared by using E_l=0.375−0.538 J/mm, corresponding to the process parameters of P= 300−350 W and v=650−800 mm/s, is appropriate, distributing in the range of 70.4−127.8 μm. This result illustrates that Cu alloys require the formation of a keyhole-mode melt pool due to the high infrared laser reflectivity, which allows the laser to be fully reflected and absorbed inside the melt pool to promote the melting of the metal powder [35,45].

A comprehensive investigation of the influence of E_l on the melt pool morphology and relative density of Cu−Cr−Nb alloy reveals that E_l affects the relative density by altering the continuity and depth of the melt pool. When the continuity of the melt pool is poor and the depth of the melt pool is too shallow, the relative density of the sample decreases. When E_l is less than 0.3 J/mm, the melt pool exhibits a pronounced balling phenomenon (Fig. 6), characterized by poor continuity and a small depth of typically less than 50 μm (Fig. 7). This corresponds to a shallow melt pool in the conduction mode, accompanied by the presence of large-sized LOF defects and unmelted powder (Figs. 3 and 4), resulting in a relative density below 95% (Fig. 5). Increasing E_l to above 0.3 J/mm improves the continuity and depth of the melt pool (Fig. 6), with a depth greater than 50 μm (Fig. 7) indicating a keyhole-mode melt pool. The number of LOF defects and unmelted powder decreases significantly (Figs. 3 and 4), leading to an increase in the relative density of the as-built alloy to 99% (Fig. 5). Further increasing E_l to more than 0.5 J/mm maintains the continuity of the melt pool (Fig. 6). However, the melt pool depth becomes excessive, exceeding 125 μm (Fig. 7), which is prone to the formation of deep keyholes (Figs. 3 and 4), resulting in a slight decrease in relative density (Fig. 5). Therefore, an excessively low or high E_l leads to the formation of pore defects and a decrease in the relative density of the as-built alloy. An appropriate E_l, from 0.375 to 0.538 J/mm, can ensure a continuous melt pool and a moderate depth, as well as reduced pore defects, which is crucial to preparing samples with high density.

3.3 Phase composition

Figure 8 presents the XRD phase analysis results of the *XY* plane for the as-built Cu−Cr−Nb−Y alloy. Figure 8(a) shows that all of the as-built alloys exhibit diffraction peaks mainly attributed to the Cu matrix, namely, the Cu (111), (200), and (220) peaks. The detailed view in Fig. 8(b) reveals the diffraction peaks of second-phase (Cr_2Nb). This indicates that rapid solidification causes the Cr and Nb elements to dissolve in the Cu matrix, forming a small amount of fine Cr_2Nb phase. Among the Cu (111), (200), and (220) diffraction peaks, the Cu (220) peak has the highest intensity, indicating a specific preferential orientation along the ⟨220⟩ direction. As the laser power increases, the intensity of the Cu (220) diffraction peak rises, while the intensities of Cu (111) and (200) diffraction peaks decrease. On the other hand, increasing the scanning speed results in a decrease in the intensity of the Cu (220) diffraction peak, while the intensities of the Cu (111) and (200) peaks increase. This suggests that reducing the laser power or increasing the scanning speed can reduce the preferred orientation of grains in the as-built alloy.

Additionally, Fig. 8(c) shows that the diffraction angles of the Cu (220) peak for all of as-built alloys are smaller than the standard diffraction angle of Cu (PDF: 97-005-3756). This suggests a slight shift toward smaller angles in the (220) diffraction peak of the as-built alloy. When v=800 mm/s, with the laser power increasing from 250 to 350 W, the diffraction angle (2θ) of the Cu (220) peak correspondingly decreases from 74.08° to 74.02°. When P=350 W, with the scanning speed increasing from 650 to 1100 mm/s, the diffraction angle of the Cu (220) peak increases from 74.02° to 74.07°.

In Fig. 8(d), the variation in interplanar spacing with laser linear energy density is depicted. It is found that with the increase in laser linear energy density, the interplanar spacing of the (111), (200), and (220) planes increases, with the maximum reaching 2.0888, 1.8111, and 1.2797 Å, respectively. The increase in laser linear energy density elevates the temperature of the melt pool during the LPBF process, which leads to an increase in the solid solubility of the Cr, Nb, and Y

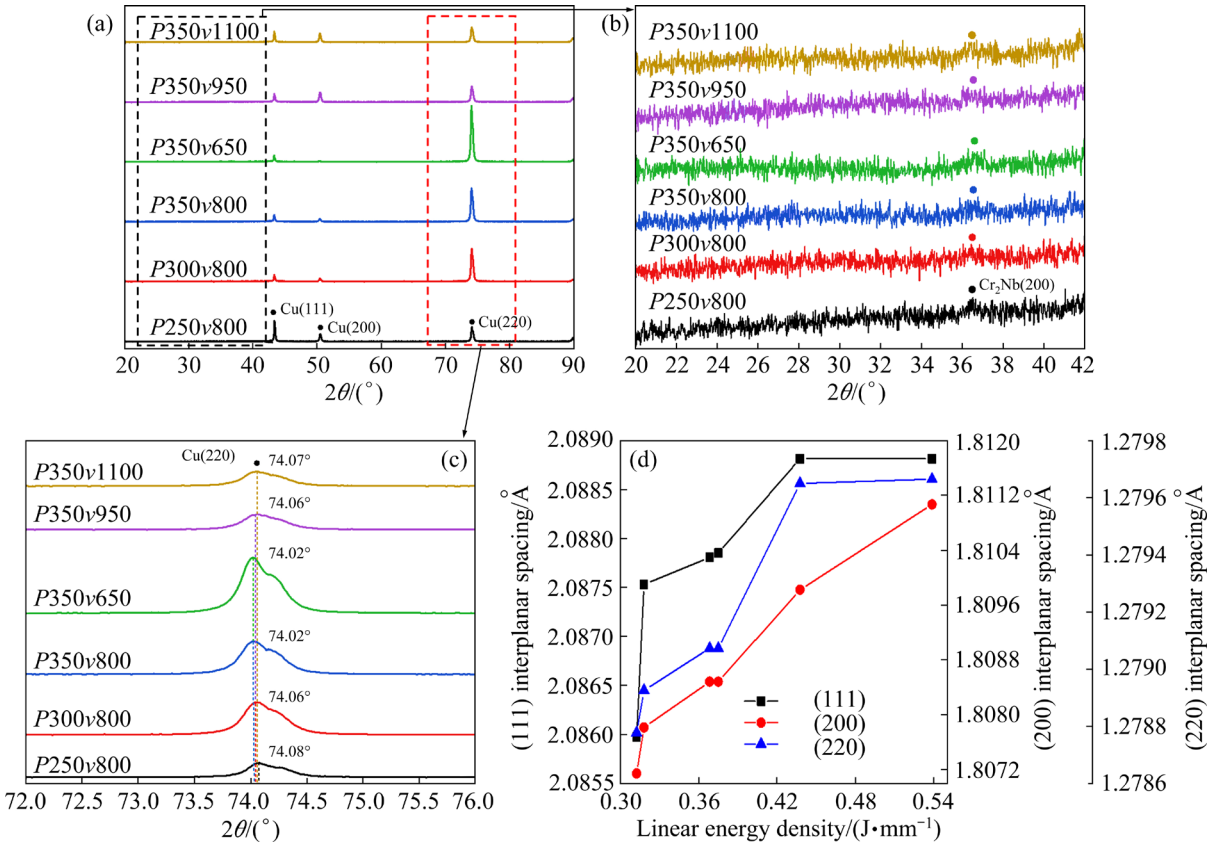

Fig. 8 XRD analysis results of as-built Cu−Cr−Nb−Y alloy: (a−c) XRD diffraction patterns; (d) (111), (200), and (220) interplanar spacing

atoms in the Cu matrix, forming a supersaturation solid solution. Since the radii of Cr, Nb, and Y atoms are larger than the radius of Cu, the lattice distortion of the Cu matrix increases, resulting in an expansion in the interplanar spacing and a slight shift in the XRD characteristic peaks toward smaller angles.

3.4 Grain size and orientation

Figure 9 shows the grain area and grain orientation of the *XY* plane in the as-built alloy fabricated with different laser powers at v= 800 mm/s. In Figures 9(a, e, i), the average grain areas of Samples *P*250*v*800, *P*300*v*800, and *P*350*v*800 are 368.1, 408.9, and 809.8 μm^2, respectively. The grain area distribution on the *XY* plane of the as-built sample exhibits a bimodal distribution, with fine grains in the center of the melt pool and coarse grains at the edge of the melt pool. Separate statistical analyses were conducted for the coarse and fine grains of as-built alloy. Figures 9(b, f, j) show that as the laser power increases, the grain area of the coarse grains grows from 572.8 to 1167.3 μm^2, indicating a significant impact of laser power on the grain size of coarse grains. On the other hand, the grain area of fine grains shows no significant change and remains around 40 μm^2, as shown in Figs. 9(c, g, k). Figures 9(d, h, l) show the pole figures (PFs) of the *XY* plane of the as-built alloy, and it is observed that as the laser power increases from 250 to 350 W, the ⟨110⟩//(001) texture intensity of the *XY* plane notably rises; moreover, the maximum texture intensity increases from 2.40 to 5.92.

Figure 10 shows the grain area and grain orientation of the *XY* plane in the as-built alloy fabricated with different laser scanning speeds at P=350 W. In Figures 10(a, e, i), it is observed that, with an increase in scanning speed, both the average grain area and the coarse grain area decrease significantly. The average grain areas of Samples *P*350*v*650, *P*350*v*950, and *P*350*v*1100 are 1067.3, 662.1, and 432.1 μm^2, respectively, while the coarse grain areas are 1343.3, 971.9, and 661.5 μm^2, respectively. Nevertheless, with the increase in scanning speed, the average grain area of fine grains exhibits no significant change and remains around 40 μm^2. Figures 10(d, h, l) illustrate that with the increase in scanning speed from 650 to 1100 mm/s, the ⟨110⟩//(001) texture intensity of the *XY* plane weakens; moreover, the maximum texture intensity decreases from 7.93 to 2.92.

Figure 11 shows the OIM maps of the *XY* plane and the corresponding distribution of

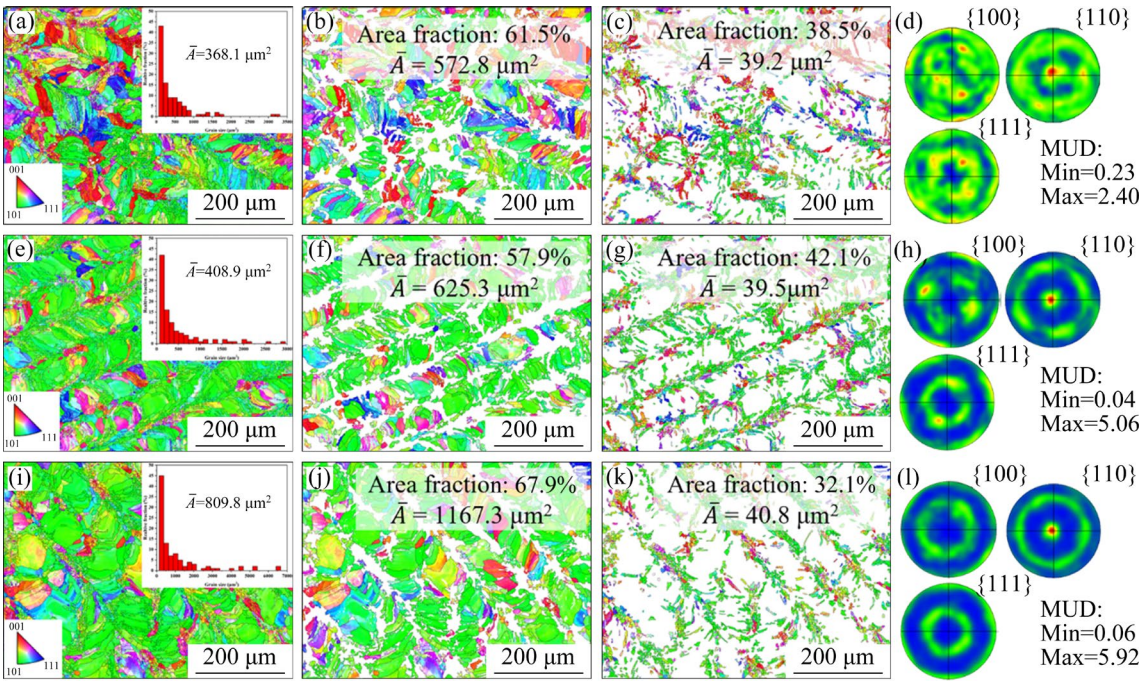

Fig. 9 Grain area and grain orientation of as-built Cu−Cr−Nb−Y alloy prepared with different laser powers at v=800 mm/s: (a−c) IPF diagrams of overall grains, coarse grains, and fine grains of Sample *P*250*v*800; (e−g) IPF diagrams of overall grains, coarse grains, and fine grains of Sample *P*300*v*800; (i−k) IPF diagrams of overall grains, coarse grains, and fine grains of Sample *P*350*v*800; (d, h, l) Corresponding PF diagrams

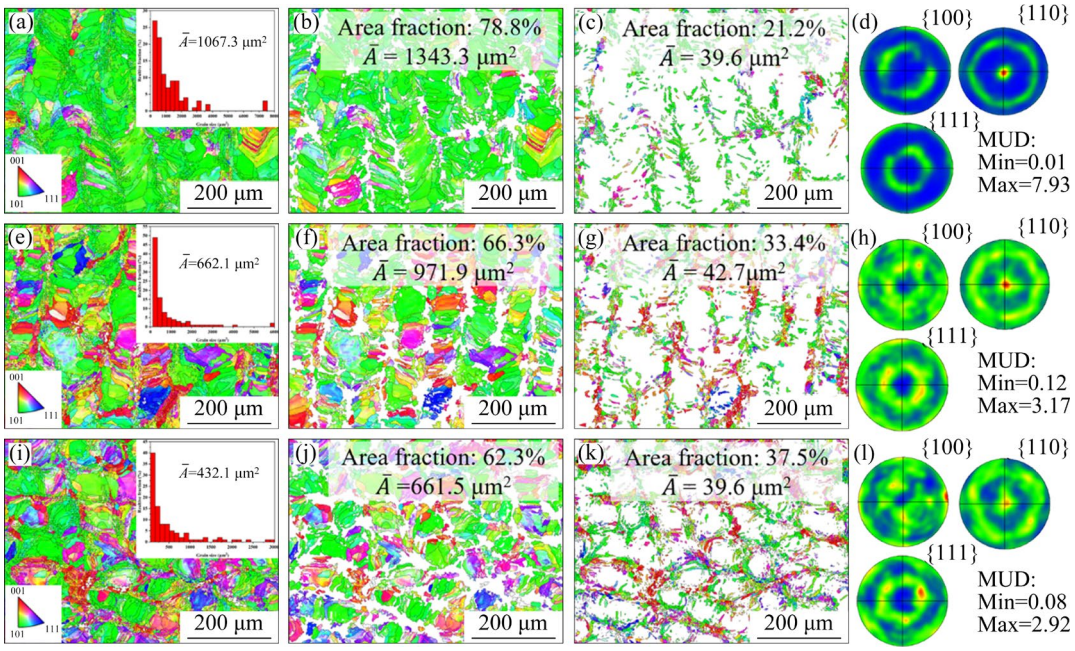

Fig. 10 Grain area and grain orientation of as-built Cu−Cr−Nb−Y alloy prepared with different scanning speeds at *P*=350 W: (a−c) IPF diagrams of overall grains, coarse grains, and fine grains of Sample *P*350*v*650; (e−g) IPF diagrams of overall grains, coarse grains, and fine grains of Sample *P*350*v*950; (i−k) IPF diagrams of overall grains, coarse grains, and fine grains of Sample *P*350*v*1100; (d, h, l) Corresponding PF diagrams

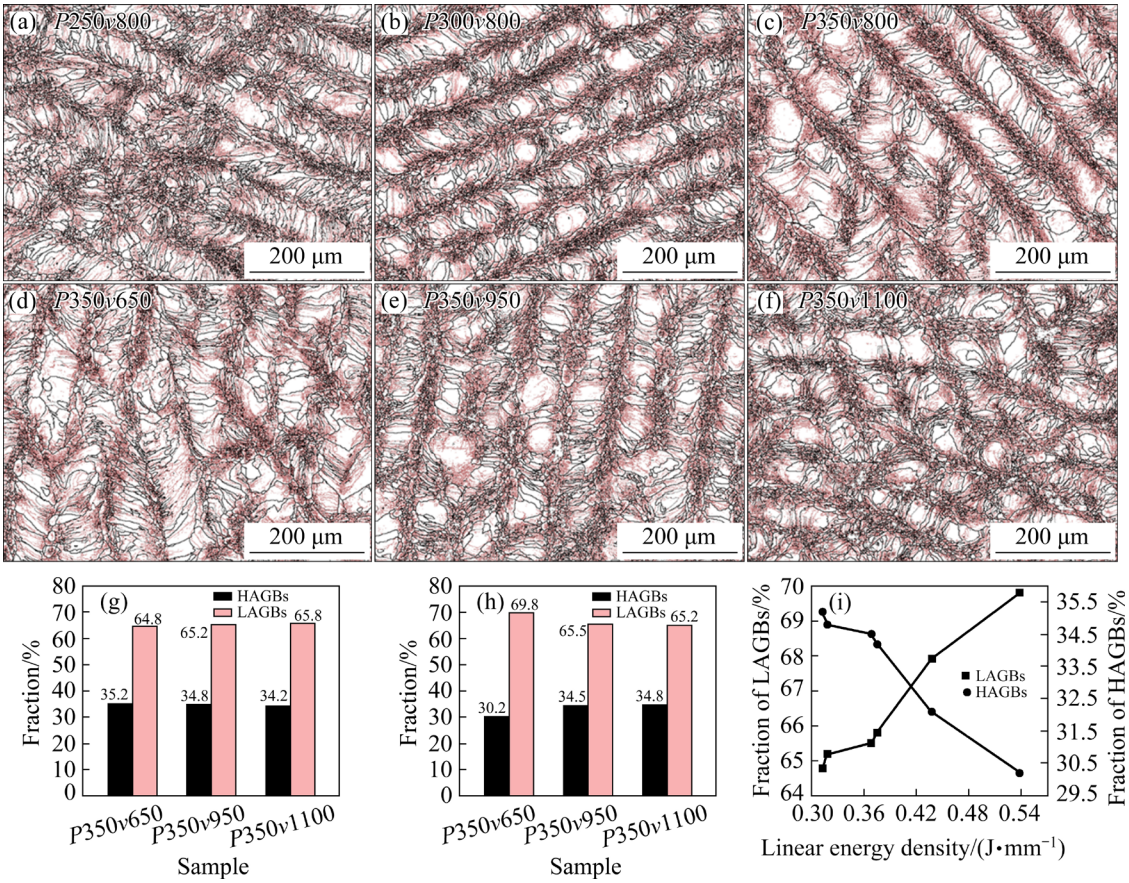

Fig. 11 OIM maps and misorientation angle distribution of as-built Cu−Cr−Nb−Y alloy: (a−c) OIM diagrams of as-built samples prepared with different laser powers (*v*=800 mm/s); (d−f) OIM diagrams of as-built samples prepared with different scanning speeds (*P*=350 W); (g−i) Statistical results of LAGBs and HAGBs of as-built samples prepared with different process parameters

orientation differences of the as-built alloy. Grain boundaries with orientation angle between 2° and 10° are defined as low-angle grain boundaries (LAGBs), which are represented in red. Conversely, grain boundaries with orientation angles greater than 10° are defined as high-angle grain boundaries (HAGBs), which are represented in black. A large number of LAGBs can be observed in all of the as-built alloy, as shown in Figs. 11(a−f), accounting for more than 60% of the total grain boundaries, primarily concentrated in the fine-grain zones. An increase in the proportion of LAGBs is associated with an increase in laser power, as shown in Fig. 11(g), whereas a decrease in the proportion of LAGBs is linked to an increase in the scanning speed, as shown in Fig. 11(h). Additionally, Fig. 11(i) shows the influence of laser linear energy density on the fraction of LAGBs and HAGBs, which indicates that with an increase in laser linear energy density, the fraction of LAGBs rises from 64.8% to 69.8%, concomitant with a decrease in the fraction of HAGBs.

Figure 12 demonstrates the microstructures of Sample *P*350*v*800. In Fig. 12(a), the melt pool tracks on the *XY* plane are visible, where adjacent melt pools overlap each other in an orderly arrangement. Figure 12(b) shows that the fine columnar grains exhibit a weak ⟨001⟩ texture along the build orientation, while the coarse grains show a distinct ⟨110⟩ texture parallel to the build orientation. In Fig. 12(c), fish-scale-like melt pools on the *XZ* plane are depicted, featuring grain epitaxial growth across the melt pools. The white dashed lines delineate the boundaries of melt pools, and the yellow arrows indicate the grain growth direction. In addition, Fig. 12(d) shows that the majority of grains on the *XZ* plane display a ⟨111⟩ texture perpendicular to the build orientation. Overall, it is found that the microstructure exhibits an alternating distribution of large- and small-sized grains, and the fine columnar grains predominantly distribute in the center of the melt pools, whereas coarse grains distribute at the edges of the melt pools.

The microstructure of the as-built Cu−Cr−Nb−Y alloy is closely related to both the thermal history and thermal gradient of the melt pool. Figure 13 illustrates the grain growth in the Cu−Cr−Nb−Y alloy during the LPBF process. In FCC metals, the ⟨001⟩ direction is the fastest growth direction of grains, and the grains grow along the direction of maximum thermal gradient [46]. During the solidification process of the melt pool, the maximum thermal gradient within the melt pool is always perpendicular to the solid/liquid interface, pointing from the edge toward the center

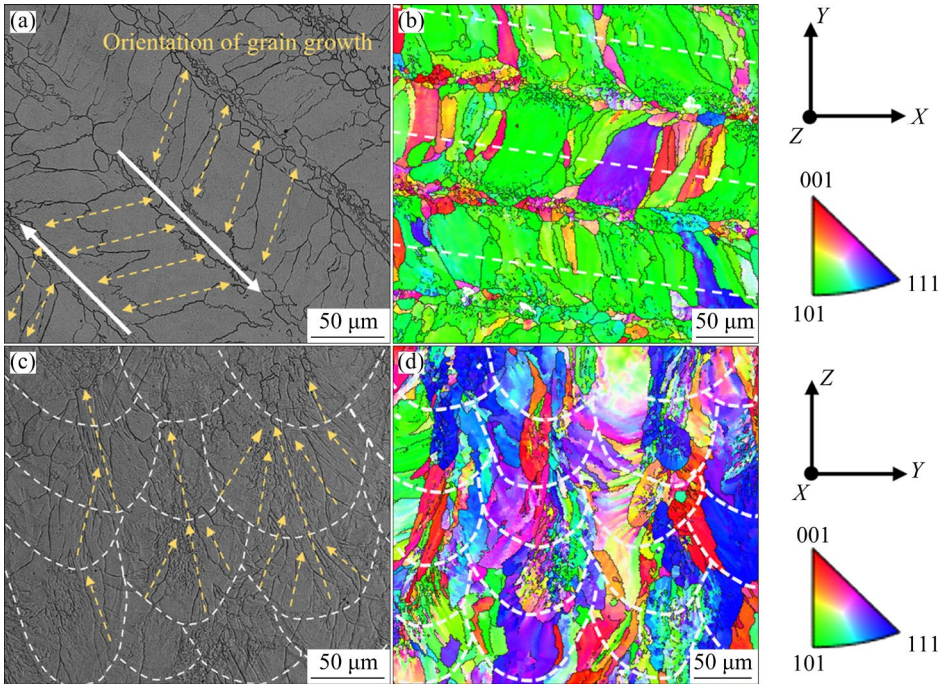

Fig. 12 Microstructure of Sample *P*350*v*800: (a, b) SEM image and IPF diagram of *XY* plane; (c, d) SEM image and IPF diagram of *YZ* plane

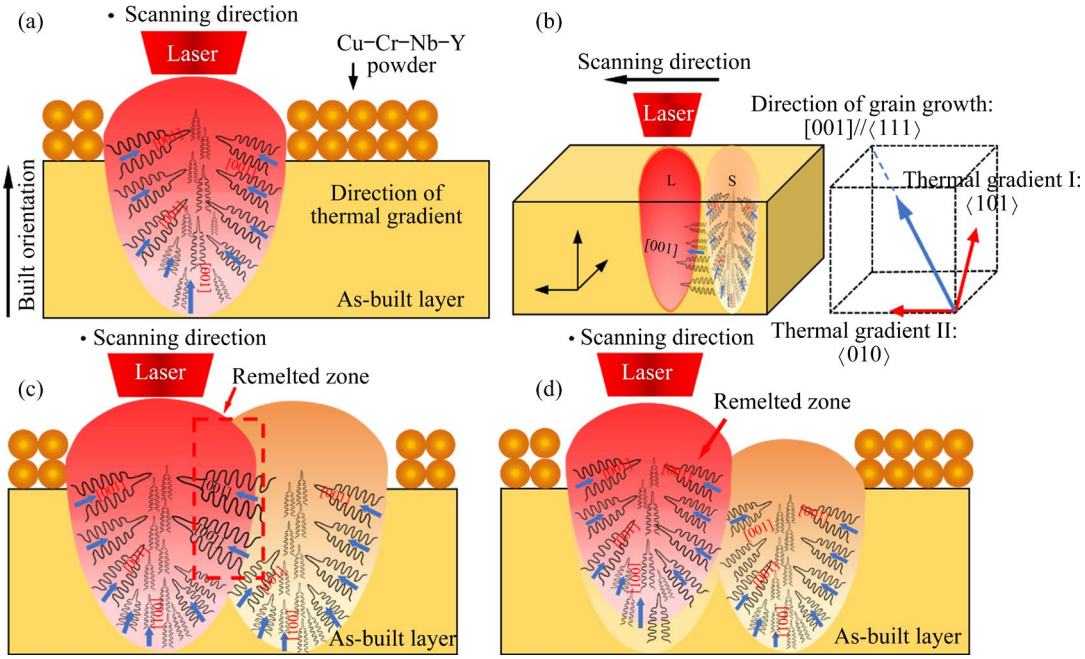

Fig. 13 Schematic diagram of grain growth during LPBF process ("S" represents solid phase and "L" represents liquid phase)

of the melt pool, represented by the blue arrow in Fig. 13(a), and the thermal gradient direction dynamically changes as the laser moves. Therefore, the grains in the center of the melt pool exhibit a weak ⟨001⟩ texture along the build orientation. Compared with other metals [47,48], the melt pool depth of the as-built Cu−Cr−Nb−Y alloy is much deeper (Fig. 7); the thermal gradient inside the melt pool rotates by a certain angle (10°−45°) relative to the bottom of melt pool [49]. The optimal growth direction deviates synchronously with the direction of the thermal gradient in the melt pool, resulting in a strong ⟨110⟩ texture parallel to the build orientation on the *XY* plane.

On account of the extremely high thermal conductivity of Cu alloys, a significant temperature gradient arises between the solid phase and liquid phase, and the direction of the thermal gradient is perpendicular to the solid/liquid interface, pointing from the solid-phase zone to the liquid-phase zone, as shown in Fig. 13(b). Therefore, the grains experience horizontal and vertical thermal gradient directions simultaneously during the LPBF process, leading to a further deviation in the grain growth direction, and ultimately, the ⟨111⟩//(001) texture is formed on the *XZ* plane, which is perpendicular to the build orientation.

During the LPBF process, a remelted zone emerges in the adjacent melt pool tracks within the same horizontal plane due to the overlapping of melt pools, as shown in Fig. 13(c). In the remelted zone, both the solid and liquid phases coexist, and epitaxial growth occurs along the horizontal direction, with the solid phase as the primary grain. In the central zone of the melt pool, the grain growth is not affected by the horizontally remelted zone, and epitaxial growth only occurs along the build orientation, as shown in Fig. 13(d), ultimately forming a bimodal grain structure with fine grains and coarse grains.

The experiment results demonstrate that the texture intensity and grain size vary with changes in the morphology of the melt pool. Specifically, changes in the melt pool depth lead to the deviation of the temperature gradient direction, causing a change in the grain growth direction and resulting in a variation in the ⟨110⟩ texture intensity on the *XY* plane. Therefore, increasing the laser power or reducing the scanning speed increases the laser linear energy density, deepening the melt pool (as shown in Fig. 7), and further changes the direction of the thermal gradient in the melt pool, ultimately leading to a change in the grain growth direction and an enhancement in the texture intensity. Conversely, the melt pool depth is shallow under low E_l conditions; moreover, the thermal gradient

direction does not experience significant deviation, resulting in a considerable proportion of grains growing parallel to the build orientation and a weaker texture intensity. Moreover, the relationship between grain size and melt pool width is closely related. With the increase in E_l, the melt pool width increases, leading to a larger partially-remelted zone between the adjacent melt pool tracks, an expanded liquid-phase zone, and more significant grain growth. Overall, the average grain area of the as-built samples prepared with various process parameters is less than 1100 μm^2, owing to the extremely high cooling rate, which facilitates grain refinement.

3.5 Mechanical properties and conductivity

Figure 14 illustrates the microhardness of Cu−Cr−Nb−Y alloy fabricated using the LPBF process, revealing a nonlinear relationship between the E_l and microhardness. With the increase in E_l, the microhardness initially increases rapidly, reaches a peak and then slightly decreases. When E_l<0.2 J/mm, the microhardness of the as-built alloy increases as E_l increases, and Sample P150v1100 (E_l=0.14 J/mm) exhibits the lowest microhardness, only $HV_{0.2}$ 174. When E_l>0.3 J/mm, the microhardness of the as-built alloy increases to over $HV_{0.2}$ 200, and the highest microhardness reaches $HV_{0.2}$ 218. Subsequently, increasing E_l to 0.5 J/mm results in a slight decrease in microhardness, ultimately being around $HV_{0.2}$ 200. It is also revealed that microhardness increases with an increase in relative density. Specifically, when the relative density exceeds 99%, the small changes in relative density no longer have a significant impact on the microhardness.

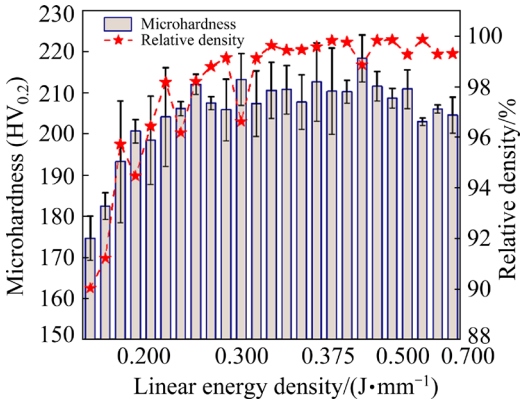

Fig. 14 Variation in microhardness and relative density of as-built Cu−Cr−Nb−Y alloy with laser linear energy density

The influence of the laser linear energy density on the microhardness is mainly achieved by affecting the porosity and microstructure of the as-built Cu–Cr–Nb–Y alloy. The microhardness can be expressed by Eqs. (3) and (4) [50]:

$$H_0=k(-\beta p^{2/3}+\gamma) \quad (3)$$

$$H_T=k\gamma \quad (4)$$

where H_0 and H_T represent the load-independent hardness and true hardness, respectively. The value of k depends on the geometric shape of the indenter, p means porosity, γ is the energy required for permanent plastic deformation per unit volume, and β is a constant. High-porosity materials are significantly affected by pore defects in terms of microhardness, and reducing the porosity leads to increased microhardness. Conversely, when the relative density exceeds 99%, microstructure plays a dominant role in microhardness, and the microhardness can be improved by refining the grain size.

As indicated by Eq. (3), the porosity has a significant impact on the load-independent hardness H_0 [50], when E_l is below 0.2 J/mm and the relative density remains below 95%. Therefore, with the increase in relative density, microhardness experiences a rapid increase. Upon increasing the laser linear energy density to 0.3 J/mm, the porosity of the sample is less than 1%, and p can be neglected; thus, the load-independent hardness H_0 is approximately equal to the true hardness H_T, and the crucial factor affecting microhardness is the energy γ, which is related to the microstructure determined by chemical composition, grain size, phase, and others of the alloy. In this study, the increase in laser linear energy density induces grain growth in the as-built alloy (Figs. 9 and 10), resulting in a decrease in microhardness.

Figure 15 shows the room-temperature tensile properties of the as-built Cu−Cr−Nb−Y alloy. Figure 15(a) represents the stress–strain curves of the as-built samples. When v=800 mm/s, increasing the laser power from 150 to 350 W results in an enhancement in both the tensile strength and elongation of the as-built samples, increasing from (439±13) MPa and (2.3±1.3)% to (699±4) MPa and(17.1±0.7)%, respectively. Conversely, when P= 250 W, increasing the scanning speed from 500 to 1100 mm/s results in a reduction in both the tensile strength and elongation of the as-built alloy,

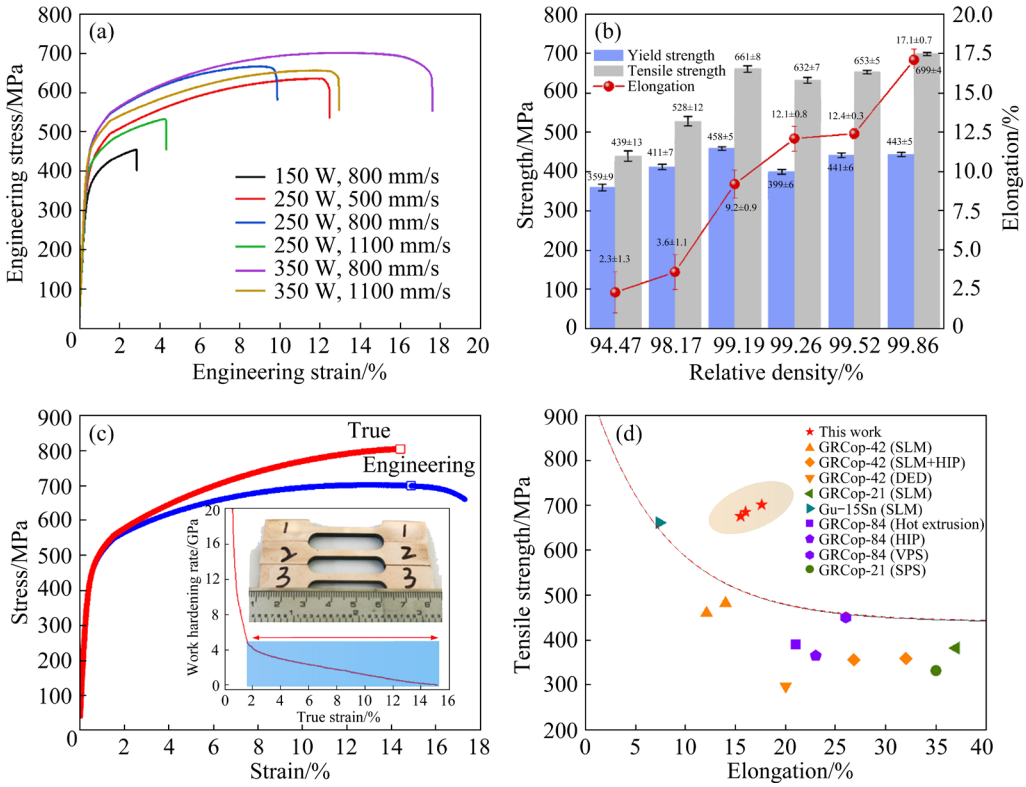

Fig. 15 Mechanical properties of as-built Cu−Cr−Nb−Y alloy: (a) Tensile curve at room temperature; (b) Variation in mechanical properties at room temperature with relative density; (c) Tensile curve and work hardening rate of Sample *P*350*v*800 at room temperature; (d) Mechanical properties of copper alloys reported in literature [51−57] and in this study

dropping from (632±7) MPa and (12.1±0.8)% to (528±12) MPa and (3.6±1.1)%, respectively. It is suggested that increasing the laser power effectively enhances the room-temperature mechanical properties, while increasing the scanning speed worsens the room-temperature mechanical properties.

Figure 15(b) shows the effect of relative density on the room-temperature tensile properties of the as-built alloy. The results indicate that the mechanical properties are enhanced with the increase in relative density. When the relative density exceeds 99%, the as-built alloy exhibits yield strength greater than 400 MPa, tensile strength above 600 MPa, and elongation exceeding 10%, demonstrating excellent mechanical properties. Sample *P*350*v*800 exhibits the best comprehensive mechanical properties, combining superior strength and ductility.

Figure 15(c) shows the true stress−strain and work hardening curves of Sample *P*350*v*800, indicating an excellent work hardening strength, reaching 255 MPa. Before the onset of plastic deformation instability, the work hardening rate remains at approximately 2 GPa, ensuring high strength and ductility simultaneously. In comparison with similar copper alloys using powder metallurgy such as hot isostatic pressing, spark plasma sintering, and vacuum hot pressing sintering [51−57], as shown in Fig. 15(d), the Cu−Cr−Nb−Y alloy prepared using the LPBF process in this study exhibits outstanding mechanical properties.

Figure 16 shows the tensile fracture morphologies of the as-built alloy. The SEM images in Figs. 16(a−c) depict the fracture morphologies of Sample *P*150*v*800, revealing the absence of a necking phenomenon. Local magnification reveals the presence of unmelted powder and large-sized pore defects, and it can be determined that these defects are attributed to LOF defects compared with Figs. 3 and 4. Figures 16(d−f) reveal the fracture morphologies of Sample *P*250*v*800, indicating a reduction in the number and size of LOF defects and unmelted powder compared with Sample *P*150*v*800.

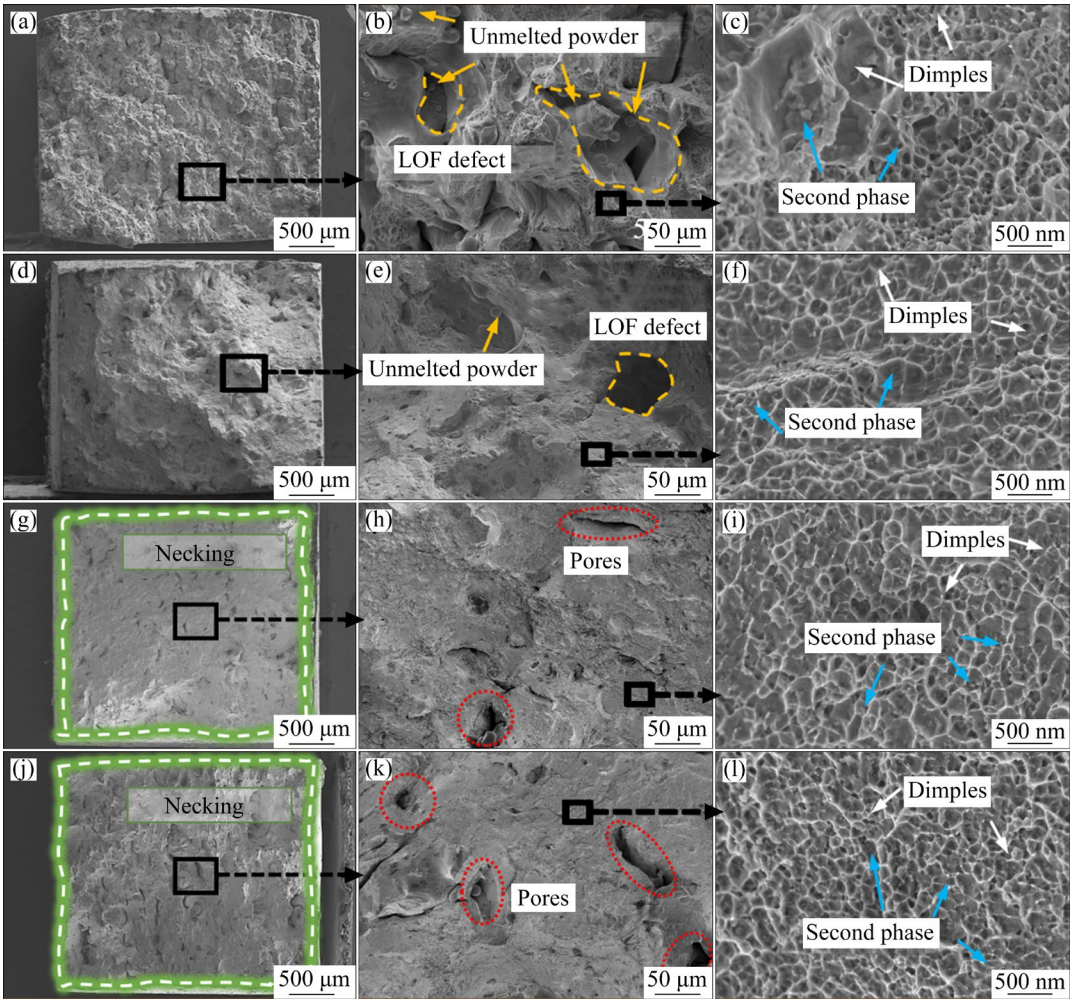

Fig. 16 Fracture morphology images of as-built Cu−Cr−Nb−Y alloy prepared with different process parameters: (a−c) P=150 W, v=800 mm/s; (d−f) P=250 W, v=800 mm/s; (g−i) P=350 W, v=800 mm/s; (j−l) P=350 W, v=1100 mm/s

Figures16(g−i) reveal the occurrence of the necking phenomenon on the fracture morphologies of Sample $P350v800$, with the disappearance of unmelted powder and large-sized pore defects. However, a certain number of small-sized pore defects emerge, which can be associated with keyholes. Figures 16(j−l) present the fracture morphologies of Sample $P350v1100$, which show that an increase in the number of pore defects and unmelted powder compared with Sample $P350v800$. High-magnification images of all sample fractures reveal small and uniform dimples, with an average size of about 200 nm. Additionally, a small amount of nano-sized second phase are discovered at the bottom of each dimple, and these nano-sized second phase hinder dislocation movement and achieve alloy strengthening during the tensile deformation. Therefore, it can be concluded that the fracture mode of all samples is ductile.

The results in Figs. 3, 15 and 16 show that the number and size of pore defects have a significant impact on the room-temperature mechanical properties of the Cu−Cr−Nb−Y alloy. An increase in the number and size of pore defects can lead to severe stress concentration during the tensile process, resulting in premature failure of the as-built alloy. With the increase in E_l, the number and size of pore defects decrease rapidly, and the strength and elongation of the alloy are improved synchronously.

Figure 17 shows the variation in conductivity of the as-built Cu−Cr−Nb−Y alloy with E_l and the relative density. It is evident that the electrical conductivity increases rapidly with the increase in E_l, and then experiences a gradual rise. Notably, Sample $P350v500$, prepared with E_l=0.7 J/mm, exhibits the highest electrical conductivity, reaching (18.6±0.2)% (IACS). When E_l<0.3 J/mm, the

relative density is below 99%, and the electrical conductivity increases with the increase in relative density. Conversely, when E_l>0.3 J/mm, the impact of the relative density on the electrical conductivity becomes negligible when the relative density surpasses 99%. The main factors governing the electrical resistivity (ρ) of copper alloys can be formulated using Eq. (5) [58]:

$$\rho=\rho_{pho}+\rho_{def}+\rho_{int}+\rho_{imp} \quad (5)$$

where ρ_{pho} represents the resistivity of phonon scattering, which is related to temperature, and therefore is excluded from consideration. ρ_{def} denotes the scattering resistance induced by the defect, including pores, grain boundaries, dislocations, vacancies, etc. ρ_{int} stands for the resistivity of interface scattering, and ρ_{imp} signifies the resistivity of impurity scattering.

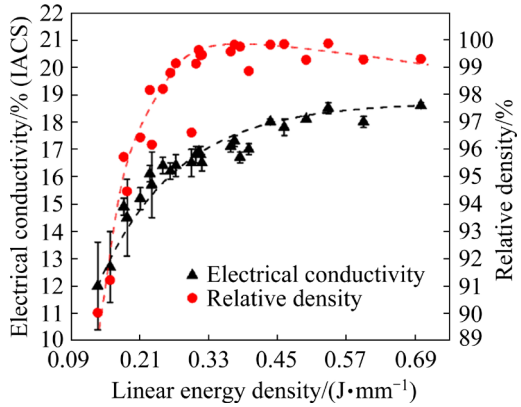

Fig. 17 Variation in electrical conductivity and relative density of as-built Cu−Cr−Nb−Y alloy with laser linear energy density

Equation (5) shows that ρ_{def}, ρ_{int}, and ρ_{imp} are essential factors affecting the electrical conductivity of copper alloys. For high porosity samples, the LOF defects significantly affect conductivity, and reducing porosity enhances conductivity. In this study, Sample *P*150*v*1100 exhibits the maximum porosity, resulting in the lowest conductivity, where the impact of electron scattering caused by porosity outweighs other factors. For samples with low porosity and relative density exceeding 99%, the influence of porosity on conductivity diminishes, and grain boundaries and impurities become the main factors affecting the conductivity. The XRD results reveal that an increase in linear energy density leads to a rise in solid solution atoms (Fig. 8), resulting in an increase in impurity scattering resistivity ρ_{imp} and a decrease in conductivity. Additionally, an increase in E_l gives rise to an increase in grain size (Figs. 9 and 10), leading to a corresponding reduction in grain boundary resistance. In this study, the variation in solid solubility of alloy elements with different parameters is limited, while the corresponding change in grain size is substantial. Therefore, grain size assumes a dominant role in conductivity. As a result, the conductivity of the as-built alloy is mainly affected by the pore defects when E_l<0.3 J/mm, and the conductivity increases with the increase in E_l. When E_l>0.3 J/mm, microstructure especially the grain size becomes the main factor, and the electrical conductivity experiences a slight increase with further increases in E_l.

4 Conclusions

(1) Process parameters have a significant influence on the defects in the as-built Cu−Cr−Nb−Y alloy, which are mainly LOF defects and keyholes. Increasing *P* or reducing *v* enhances the continuity of the melt pool, resulting in a rapid reduction in the number of LOF defects and unmelted powder, accompanied by an increase in the relative density of the alloy. The as-built alloy with E_l<0.3 J/mm are mainly characterized by LOF defects, while the as-built alloy with E_l>0.5 J/mm have excessively deep melt pools, resulting in a sharp increase in the number of keyholes. The optimized process parameters for preparing the Cu−Cr−Nb−Y alloy using the LPBF process are *P*=300−350 W and *v*=650−800 mm/s. By using *P*=350 W and *v*=800 mm/s, the melt pool with good continuity and an appropriate depth of 96.7 μm can be prepared, resulting in sample with the highest relative density of 99.82%. The E_l can only be used as a reference parameter for Cu−Cr−Nb−Y alloys manufactured using the LPBF process.

(2) The microstructure of the as-built alloy consists of a Cu supersaturated solid solution and a small Cr_2Nb phase, which exhibits fine grains in the center of the melt pool and coarse grains at the edge, with a bimodal distribution of grain sizes. The *XY* plane of the as-built alloy demonstrates an intense ⟨110⟩//(001) texture. Increasing *P* or reducing *v* amplifies the melt pool depth, as well as expanding the melt pool width and remelted zone, which intensifies the ⟨110⟩//(001) texture intensity and

increases the grain size on the *XY* plane.

(3) The mechanical properties and electrical conductivity are influenced by the defects and microstructure, which are determined by the process parameters. Increasing E_l enhances the mechanical properties and electrical conductivity. However, excessive E_l leads to a slight decrease in microhardness owing to the increased grain size. The Cu−Cr−Nb−Y alloy prepared with parameters P=350 W and v=800 mm/s demonstrates the optimal room-temperature tensile properties, with YS, UTS, and elongation of (443±5) MPa, (699±4) MPa, and (17.1±0.7)%, respectively.

CRediT authorship contribution statement

Shu-peng YE: Investigation, Methodology, Formal analysis, Data curation, Writing − Original draft, Writing − Review & editing; **Zu-ming LIU:** Writing – Review & editing, Methodology, Data curation, Funding acquisition, Supervision; **Ya-zhou ZHANG:** Methodology; **Tao LIU** and **Dao-yan JIANG:** Methodology; **Lei CHEN:** Methodology, Formal analysis; **Cai CHEN:** Formal analysis.

Declaration of competing interest

The authors declare that they have no known competing financial interests or personal relationships that could have appeared to influence the work reported in this paper.

Acknowledgments

This work was financially supported by the Project of Chinese Academy of Engineering (Nos. 2019-XZ-11 and 2023-XY-18), and the Open Fund of National Joint Engineering Research Center for Abrasion Control and Molding of Metal Materials of China (No. HKDNM201907). The authors would like to thank Prof. Jin-zhi TANG for reviewing this paper and Prof. Yun-fei HUANG for language help.

References

[1] YANG Hui-ya, MA Zi-chao, LEI Chen-hui, MENG Liang, FANG You-tong, LIU Jia-bin, WANG Hong-tao. High strength and high conductivity Cu alloys: A review [J]. Science China Technological Sciences, 2020, 63: 2505−2517.

[2] XIA Cheng-dong, ZHANG Wan, KANG Zhan-yuan, JIA Yan-lin, WU Yi-feng, ZHANG Rui, XU Gen-ying, WANG Ming-pu. High strength and high electrical conductivity Cu−Cr system alloys manufactured by hot rolling–quenching process and thermomechanical treatments [J]. Materials Science and Engineering A, 2012, 538: 295−301.

[3] LEI Q, LI Z, WANG M P, ZHANG L, XIAO Z, JIA Y L. The evolution of microstructure in Cu−8.0Ni−1.8Si−0.15Mg alloy during aging [J]. Materials Science and Engineering A, 2010, 527: 6728−6733.

[4] MINNECI R P, LASS E A, BUNN J R, CHOO H, RAWN C J. Copper-based alloys for structural high-heat-flux applications: A review of development, properties, and performance of Cu-rich Cu−Cr−Nb alloys [J]. International Materials Reviews, 2020, 66: 394−425.

[5] LEI Qian, YANG Yi-hai, XIAO Zhu, JIANG Yan-bin, GONG Shen, LI Zhou. Research progress and prospect on high strength, high conductivity, and high heat resistance copper alloys [J]. Materials Reports, 2021, 35: 15153−15161. (in Chinese)

[6] ELLIS D L. GRCop-84: A high temperature copper-based alloy for high heat flux applications [R]. Cleveland, Ohio: Glenn Research Center, National Aeronautics and Space Administration, 2005.

[7] DHOKEY N B, SARVE S N, LAMSOGE H A. Development of in-situ synthesis of Cr_2Nb reinforced copper alloy by aluminothermic process [J]. Transactions of the Indian Institute of Metals, 2011, 64: 425−429.

[8] DHOKEY N B, SARVE S N, LAMSOGE H A. In situ synthesis of Cr_2Nb reinforced copper alloy by liquid metallurgy route [J]. Materials Science Forum, 2012, 710: 143−148.

[9] ELLIS D L, MICHAL G M. Precipitation strengthened high strength, high conductivity Cu−Cr−Nb alloys produced by chill block melt spinning [R]. Cleveland, Ohio: Lewis Research Center, National Aeronautics and Space Administration, 1989.

[10] ANDERSON K R. Effects of thermal and mechanical processing on microstructures and desired properties of particle-strengthened Cu−Cr−Nb alloys [R]. Cleveland, Ohio: Glenn Research Center, National Aeronautics and Space Administration, 2000.

[11] ANDERSON K R, GROZA J R, DRESHFIELD R L, ELLIS D. Microstructural evolution and thermal stability of precipitation-strengthened Cu8Cr4Nb alloy [J]. Materials Science and Engineering A, 1993, 169: 167−175.

[12] ANDERSON K R, GROZA J R, DRESHFIELD R L, ELLIS D. High-performance dispersion-strengthened Cu−8Cr−4Nb alloy [J]. Metallurgical and Materials Transactions A, 1995, 26: 2197−2206.

[13] GROZA J R. Microstructural features of a new precipitation-strengthened Cu8Cr4Nb alloy [J]. Materials Characterization, 1993, 31: 133−141.

[14] LIU Guo, ZHANG Xiao-feng, CHEN Xu-liang, HE Yun-hu, CHENG Li-zi, HUO Meng-ke, YIN Jian-an, HAO Feng-qian, CHEN Si-yao, WANG Pei-yu, YI Sheng-hui, WAN Lei, MAO Zheng-yi, CHEN Zhou, WANG Xu, CAO Zhao-wen-bo, LU Jian. Additive manufacturing of structural materials [J]. Materials Science and Engineering R: Reports, 2021, 145: 100596.

[15] YANG Xu, QI Yang, ZHANG Wen-qi, WANG Yi-long, ZHU Hai-hong. Laser powder bed fusion of C18150 copper alloy with excellent comprehensive properties [J]. Materials Science and Engineering A, 2023, 862: 144512.

[16] YANG Xu, WANG Yi-long, ZHANG Wen-qi, QI Yang, ZHANG Bao-peng, ZHANG Hu, ZHU Hai-hong. Laser powder bed fusion fabricated Cu−1.8Cr−1.0Nb−2.0Fe alloy

with in-situ precipitation strengthening [J]. Materials Science and Engineering A, 2023, 878: 145222.

[17] HOOPER P A. Melt pool temperature and cooling rates in laser powder bed fusion [J]. Additive Manufacturing, 2018, 22: 548−559.

[18] GRADL P R, PROTZ C S, ELLIS D L, GREENE S E. Progress in additively manufactured copper-alloy GRCop-84, GRCop-42, and bimetallic combustion chambers for liquid rocket engines [C]//70th International Astronautical Congress (IAC). Washington DC, United States: IAC, 2019: 1−14.

[19] SELTZMAN A H, WUKITCH S J. Fracture characteristics and heat treatment of laser powder bed fusion additively manufactured GRCop-84 copper [J]. Materials Science and Engineering A, 2021, 827: 141690.

[20] TRAN T Q, CHINNAPPAN A, LEE J K Y, LOC N H, TRAN L T, WANG Geng-jie, KUMAR V V, JAYATHILAKA W A D M, JI Dong-xiao, DODDAMANI M, RAMAKRISHNA S. 3D printing of highly pure copper [J]. Metals, 2019, 9: 756.

[21] GRADL P R, PROTZ C, GREENE S E, ELLIS D, LERCH B, LOCCI I. Development and hot-fire testing of additively manufactured copper combustion chambers for liquid rocket engine applications [C]//53rd AIAA/SAE/ASEE Joint Propulsion Conference. Atlanta, GA: AIAA, 2017: 1−27.

[22] LV Xue-qian, LIU Zu-ming, LEI Ting, LI Quan, ZHAO Fan, PENG Kai, REN Ya-ke, LU Si-zhe, NONG Bi-zhong. Microstructure and properties of Cu−Cr−Nb alloy powder prepared by argon gas atomization [J]. Advanced Powder Technology, 2019, 30: 2464−2472.

[23] LIANG Dong, MI Xu-jun, PENG Li-jun, XIE Hao-feng, HUANG Guo-jie, YANG Zhen. Relationship between microstructure and properties of Cu−Cr−Ag alloy [J]. Materials, 2020, 13: 732.

[24] LI Hai-hong, LIU Xiao, LI Yang, ZHANG Shi-hong, CHEN Yan, WANG Song-wei, LIU Jin-song, WU Jin-hu. Effects of rare earth Ce addition on microstructure and mechanical properties of impure copper containing Pb [J]. Transactions of Nonferrous Metals Society of China, 2020, 30: 1574−1581.

[25] ZHANG Yi, CHAI Zhe, VOLINSKY A A, TIAN Bao-hong, SUN Hui-li, LIU Ping, LIU Yong. Processing maps for the Cu−Cr−Zr−Y alloy hot deformation behavior [J]. Materials Science and Engineering A, 2016, 662: 320−329.

[26] BERTOLI U S, WOLFER A J, MATTHEWS M J, DELPLANQUE J R, SCHOENUNG J M. On the limitations of volumetric energy density as a design parameter for selective laser melting [J]. Materials & Design, 2017, 113: 331−340.

[27] OLAKANMI E O. Selective laser sintering/melting (SLS/SLM) of pure Al, Al−Mg, and Al−Si powders: Effect of processing conditions and powder properties [J]. Journal of Materials Processing Technology, 2013, 213: 1387−1405.

[28] QI Yang, ZHANG Hu, NIE Xiao-jia, HU Zhi-heng, ZHU Hai-hong, ZENG Xiao-yan. A high strength Al−Li alloy produced by laser powder bed fusion: Densification, microstructure, and mechanical properties [J]. Additive Manufacturing, 2020, 35: 101346.

[29] QI Yang, HU Zhi-heng, ZHANG Hu, NIE Xiao-jia, ZHANG Chang-chun, ZHU Hai-hong. High strength Al−Li alloy development for laser powder bed fusion [J]. Additive Manufacturing, 2021, 47: 102249.

[30] GURAYA T, SINGAMNENI S, CHEN Z W. Microstructure formed during selective laser melting of IN738LC in keyhole mode [J]. Journal of Alloys and Compounds, 2019, 792: 151−160.

[31] HU Yong, YANG Xiao-kang, KANG Wen-jiang, DING Yu-tian, XU Jia-yu, ZHANG Hui-ying. Effect of Zr content on crack formation and mechanical properties of IN738LC processed by selective laser melting [J]. Transactions of Nonferrous Metals Society of China, 2021, 31: 1350−1362.

[32] YUE Tian-yang, ZHANG Sheng, WANG Chao-yue, XU Wei, XU Yi-di, SHI Yu-sheng, ZHANG Yong. Effects of selective laser melting parameters on surface quality and densification behaviours of pure nickel [J]. Transactions of Nonferrous Metals Society of China, 2022, 32: 2634−2647.

[33] GONG Hai-jun, GU Heng-feng, ZENG Kai, DILIP J J S, PAL D, STUCKER B. Melt pool characterization for selective laser melting of Ti−6Al−4V pre-alloyed powder [C]//2014 International Solid Freeform Fabrication Symposium. Austin: University of Texas, 2014: 256−267.

[34] AN Na-ying, SHUAI San-san, CHEN Chao-yue, LEI Li-ming, WWANG Jiang, REN Zhong-ming. Quantitative study of geometric characteristics and formation mechanism of porosity defects in selective laser melted Ti6Al4V alloy by micro-computed tomography [J]. Transactions of Nonferrous Metals Society of China, 2023, 33: 2986−3002.

[35] JADHAV S D, GOOSSENS L R, KINDS Y, HOOREWEDER B V, VANMEENSEL K. Laser-based powder bed fusion additive manufacturing of pure copper [J]. Additive Manufacturing, 2021, 42: 101990.

[36] LI Jian, LIU Zu-ming, ZHOU Huan, YE Shu-peng, ZHANG Ya-zhou, LIU Tao, JIANG Dao-yan, CHEN Lei, ZHOU Run-xing. Effect of process parameters on the microstructure and properties of Cu−Cr−Nb−Ti alloy manufactured by selective laser melting [J]. Materials, 2023, 16: 2912.

[37] ISO 12154:2014. Determination of density by volumetric displacement-Skeleton density by gas pycnometry [S]. London, UK, 2014.

[38] WANG Shu-hao, NING Jin-sheng, ZHU Li-da, YANG Zhi-chao, YAN Wen-tao, DUN Yi-chao, XUE Peng-sheng, XU Pei-hua, BOSE S, BANDYOPADHYAY A. Role of porosity defects in metal 3D printing: Formation mechanisms, impacts on properties and mitigation strategies [J]. Materials Today, 2022, 59: 133−160.

[39] KASPEROVICH G, HAUBRICH J, GUSSONE J, REQUENA G. Correlation between porosity and processing parameters in TiAl6V4 produced by selective laser melting [J]. Materials & Design, 2016, 105: 160−170.

[40] FERRO P, MENEGHELLO R, SAVIO G, BERTO F. A modified volumetric energy density–based approach for porosity assessment in additive manufacturing process design [J]. The International Journal of Advanced Manufacturing Technology, 2020, 110: 1911−1921.

[41] CUNNINGHAM R, ZHAO Cang, PARAB N, KANTZOS C, PAUZA J, FEZZAA K, SUN Tao, ROLLETT A D. Keyhole threshold and morphology in laser melting revealed by ultrahigh-speed X-ray imaging [J]. Science, 2019, 363: 849−852.

[42] ZHAO Cang, PARAB N D, LI Xu-xiao, FEZZAA K, TAN Wen-da, ROLLETT A D, SUN Tao. Critical instability at moving keyhole tip generates porosity in laser melting [J]. Science, 2020, 370: 1080−1086.

[43] LI Rui-di, LIU Jin-hui, SHI Yu-sheng, WANG Li, JIANG Wei. Balling behavior of stainless steel and nickel powder during selective laser melting process [J]. The International Journal of Advanced Manufacturing Technology, 2012, 59: 1025−1035.
[44] LU Liang-xing, SRIDHAR N, ZHANG Yong-wei. Phase field simulation of powder bed-based additive manufacturing [J]. Acta Materialia, 2018, 144: 801−809.
[45] TRAPP J, RUBENCHIK A M, GUSS G, MATTHEWS M J. In situ absorptivity measurements of metallic powders during laser powder-bed fusion additive manufacturing [J]. Applied Materials Today, 2017, 9: 341−349.
[46] KOU S. Welding metallurgy [M]. 2nd ed. Hoboken: Wiley, 2003.
[47] BAUMARD A, AYRAULT D, FANDEUR O, BORDREUIL C, DESCHAUX-BEAUME F. Numerical prediction of grain structure formation during laser powder bed fusion of 316 L stainless steel [J]. Materials & Design, 2021, 199: 109434.
[48] CHEN Dong-ju, LI Gang, WANG Peng, ZENG Zhi-qiang, TANG Yu-hang. Numerical simulation of melt pool size and flow evolution for laser powder bed fusion of powder grade Ti6Al4V [J]. Finite Elements in Analysis and Design, 2023, 223: 103971.
[49] JADHAV S D, DADBAKHSH S, GOOSSENS L, KRUTH J P, HUMBEECK J V, VANMEENSEL K. Influence of selective laser melting process parameters on texture evolution in pure copper [J]. Journal of Materials Processing Technology, 2019, 270: 47−58.
[50] TANG Qi, GONG Jiang-hong. Effect of porosity on the microhardness testing of brittle ceramics: A case study on the system of NiO−ZrO_2 [J]. Ceramics International, 2013, 39: 8751−8759.
[51] GRADL P R, PROTZ C S, COOPER K, ELLIS D, EVANS L J, GARCIA C. GRCop-42 development and hot-fire testing using additive manufacturing powder bed fusion for channel-cooled combustion chambers [C]//55th AIAA Propulsion and Energy 2019 Forum. Indianapolis, Indiana: AIAA, 2019: 1−26.
[52] COOPER K G, LYDON J L, LECORRE M D, JONES Z C, SCANNAPIECO D S, ELLIS D L, LERCH B A. Three-dimensional printing GRCop-42 [R]. Huntsville, Alabama: Marshall Space Flight Center, National Aeronautics and Space Administration, 2018.
[53] ELLIS D L, LOEWENTHAL W S, YUN H M. Tensile properties of GRCop-84 [R]. Cleveland, Ohio: Glenn Research Center, National Aeronautics and Space Administration, 2012.
[54] ELLIS D L. Mechanical properties of Cu−Cr−Nb alloys [R]. Cleveland, Ohio: Lewis Research Center, National Aeronautics and Space Administration, 1997.
[55] REN Ya-ke, LÜ Xue-qian, LIU Zu-ming, WEI Bing, LEI Ting, LI Quan, JI Xiao-bo, DENG Wen-tao, AI Yong-kang. Microstructure and properties of Cu−2Cr−1Nb alloy fabricated by spark plasma sintering [J]. Transactions of Nonferrous Metals Society of China, 2022, 32: 2276−2289.
[56] LANDES S, SURESH T, PRASAD A, LETCHER T, GRADL P, ELLIS D. Investigation of additive manufactured GRCop-42 alloy developed by directed energy deposition methods [C]//ASME 2020 International Mechanical Engineering Congress and Exposition. Portland, OR, USA: IMECE, 2020: 1−7.
[57] MAO Zhong-fa, ZHANG D Z, JIANG Jun-jie, FU Guang, ZHANG Peng. Processing optimisation, mechanical properties and microstructural evolution during selective laser melting of Cu−15Sn high-tin bronze [J]. Materials Science and Engineering A, 2018, 721: 125−134.
[58] QU Lei, WANG En-gang, HAN Ke, ZUO Xiao-wei, ZHANG Lin, JIA Peng, He Ji-cheng. Studies of electrical resistivity of an annealed Cu−Fe composite [J]. Journal of Applied Physics, 2013, 113: 173708.

激光粉末床熔融工艺参数对 Cu−Cr−Nb−Y 合金显微组织与性能的影响

叶书鹏，刘祖铭，张亚洲，刘 涛，江道言，陈 雷，陈 才

中南大学 粉末冶金全国重点实验室，长沙 410083

摘 要：采用激光粉末床熔融技术制备了 Cu−4.8Cr−2.2Nb−0.15Y (摩尔分数，%)合金。系统研究了激光功率(P)、扫描速度(v)和激光线能量密度(E_l)等工艺参数对合金缺陷、熔池形貌、显微组织及性能的影响。结果表明，制备相对密度超过 99.5%的 Cu−Cr−Nb−Y 合金的最佳工艺参数为 P=300~350 W 和 v=650~800 mm/s，对应于 E_l=0.375~0.538 J/mm。当 E_l<0.3 J/mm 时，提高 P 或降低 v 可以增加熔池的连续性和尺寸，减少未熔合缺陷，提高相对密度。然而，过高的 E_l 导致熔池深度过深，锁孔数量增加，相对密度降低。制备的 Cu−Cr−Nb−Y 合金的晶粒尺寸呈双峰分布，熔池中心为细晶，熔池边缘为粗晶。增加 P 或减少 v 可增加平均晶粒尺寸和⟨110⟩织构的强度。采用 P=350 W 和 v=800m/s 制备的合金相对密度最高，达 99.82%，样品的屈服强度、抗拉强度和伸长率分别为(443±5) MPa、(699±4) MPa 和(17.1±0.7)%。

关键词：Cu−Cr−Nb−Y 合金；激光粉末床熔融；熔池形态；显微组织；力学性能

(Edited by Bing YANG)